Multidiscipline Modeling in Materials and Structures

Emerald Article: Computational investigation of shock-mitigation efficacy of polyurea when used in a combat helmet: A core sample analysis

M. Grujicic, A. Arakere, B. Pandurangan, A. Grujicic, A. Littlestone, R. Barsoum

Report Documentation Page

Form Approved
OMB No. 0704-0188

1. REPORT DATE	2. REPORT TYPE	3. DATES COVERED
2012		**00-00-2012 to 00-00-2012**

4. TITLE AND SUBTITLE
Computational investigation of shock-mitigation efficacy of polyurea when used in a combat helmet: A core sample analysis

5a. CONTRACT NUMBER
5b. GRANT NUMBER
5c. PROGRAM ELEMENT NUMBER

6. AUTHOR(S)

5d. PROJECT NUMBER
5e. TASK NUMBER
5f. WORK UNIT NUMBER

7. PERFORMING ORGANIZATION NAME(S) AND ADDRESS(ES)
Clemson University,Department of Mechanical Engineering,241 Engineering Innovation Building,Clemson,SC,29634

8. PERFORMING ORGANIZATION REPORT NUMBER

9. SPONSORING/MONITORING AGENCY NAME(S) AND ADDRESS(ES)

10. SPONSOR/MONITOR'S ACRONYM(S)
11. SPONSOR/MONITOR'S REPORT NUMBER(S)

12. DISTRIBUTION/AVAILABILITY STATEMENT
Approved for public release; distribution unlimited

13. SUPPLEMENTARY NOTES

14. ABSTRACT

Purpose ? Polyurea falls into a category of elastomeric co-polymers in which, due to the presence of strong hydrogen bonding, the microstructure is of a heterogeneous nature and consists of a compliant/soft matrix and stiff/hard nanometer size hard domains. Recent investigations have shown that the use of polyurea as an external or internal coating/lining had substantially improved ballistic-penetration resistance of metallic structures. The present work aims to use computational methods and tools in order to assess the shock-mitigation ability of polyurea when used in the construction of different components (suspension-pads, internal lining and external coating) of a combat helmet. Design/methodology/approach ? Shock-mitigation capability of combat helmets has become an important functional requirement as shock-ingress into the intra-cranial cavity is known to be one of the main causes of traumatic brain injury (TBI). To assess the shock mitigation capability of polyurea a combined Eulerian/Lagrangian fluid/solid transient non-linear dynamics computational analysis of an air/helmet/head core sample is carried out and the temporal evolution of the axial stress and particle velocities (for different polyurea augmented helmet designs) are monitored. Findings ? The results obtained show that improvements in the shock-mitigation performance of the helmet are obtained only in the case when polyurea is used as a helmet internal lining and that these improvements are relatively small. In addition, polyurea is found to slightly outperform conventional helmet foam, but only under relatively strong (greater than five atm) blastwave peak overpressures. Originality/value ? The present approach studies the effect of internal linings and external coatings on combat helmet blast mitigation performance.

15. SUBJECT TERMS

16. SECURITY CLASSIFICATION OF:			17. LIMITATION OF ABSTRACT	18. NUMBER OF PAGES	19a. NAME OF RESPONSIBLE PERSON
a. REPORT **unclassified**	b. ABSTRACT **unclassified**	c. THIS PAGE **unclassified**	**Same as Report (SAR)**	**36**	

Standard Form 298 (Rev. 8-98)
Prescribed by ANSI Std Z39-18

The current issue and full text archive of this journal is available at
www.emeraldinsight.com/1573-6105.htm

Computational investigation of shock-mitigation efficacy of polyurea when used in a combat helmet

A core sample analysis

Received 15 December 2011
Revised 7 February 2012
Accepted 9 February 2012

M. Grujicic and A. Arakere
Clemson University, Clemson, South Carolina, USA
B. Pandurangan
Corvid Technologies, Mooresville, North Carolina, USA
A. Grujicic
Clemson University, Clemson, South Carolina, USA
A. Littlestone
Naval Surface Warfare Center, Carderock Division, West Bethesda, Maryland, USA, and
R. Barsoum
Office of Naval Research, Arlington, Virginia, USA

Abstract

Purpose – Polyurea falls into a category of elastomeric co-polymers in which, due to the presence of strong hydrogen bonding, the microstructure is of a heterogeneous nature and consists of a compliant/soft matrix and stiff/hard nanometer size hard domains. Recent investigations have shown that the use of polyurea as an external or internal coating/lining had substantially improved ballistic-penetration resistance of metallic structures. The present work aims to use computational methods and tools in order to assess the shock-mitigation ability of polyurea when used in the construction of different components (suspension-pads, internal lining and external coating) of a combat helmet.

Design/methodology/approach – Shock-mitigation capability of combat helmets has become an important functional requirement as shock-ingress into the intra-cranial cavity is known to be one of the main causes of traumatic brain injury (TBI). To assess the shock mitigation capability of polyurea, a combined Eulerian/Lagrangian fluid/solid transient non-linear dynamics computational analysis of an air/helmet/head core sample is carried out and the temporal evolution of the axial stress and particle velocities (for different polyurea augmented helmet designs) are monitored.

Findings – The results obtained show that improvements in the shock-mitigation performance of the helmet are obtained only in the case when polyurea is used as a helmet internal lining and that these improvements are relatively small. In addition, polyurea is found to slightly outperform conventional helmet foam, but only under relatively strong (greater than five atm) blastwave peak overpressures.

Originality/value – The present approach studies the effect of internal linings and external coatings on combat helmet blast mitigation performance.

Keywords Polyurea, Shock mitigation, Combat helmet, Force, Strength of materials

Paper type Research paper

Multidiscipline Modeling in Materials and Structures
Vol. 8 No. 3, 2012
pp. 297-331

1573-6105
DOI 10.1108/15736101211269122

1. Introduction

The main objective of the present work is to examine (computationally) shock-mitigation efficacy (critical from the standpoint of reducing the potential for traumatic brain injury (TBI) during exposure to blast loading) of polyurea when this elastomeric material is utilized in the construction of different components of a head protection system (a helmet). Hence, the key aspects of the present work are:

- polyurea;
- TBI; and
- design of currently-used helmets.

These aspects will be briefly overviewed in the remainder of this section.

Polyurea

Polyurea falls into a class of microphase-segregated and thermoplastically cross-linked elastomeric co-polymers (the terms "microphase-segregated" and "thermoplastically cross-linked" will be defined later) that are formed by the rapid chemical reaction between isocyanates (organic chemicals containing isocyanate —N═C═O groups) and amines (organic chemicals containing amine $-NH_2$ groups). There are two aspects of this material which are often cited as being particularly attractive:

(1) the co-polymerization/gel reaction times are typically less than a minute so that this material can be produced using a spraying process; and

(2) a variety of microstructures can be obtained through small variations in the chemistry and/or synthesis conditions.

Examination of the structure of polyurea molecules/chains shows the presence of urea linkages (—NH—CO—NH—) which are polar (i.e. contain centers/poles of negative and positive charge) and together with the adjoining di-phenyl methane ($C_6H_5—CH_2—C_6H_5$) functional groups form the so-called "hard (i.e. high-stiffness) segments". Within the same molecule, various aliphatic functional groups form the so-called "soft (i.e. low stiffness) segments". As a result of strong hydrogen bonding between urea linkages of the neighboring chains (or the neighboring portions of the same chain), hard segments are typically micro-phase segregated into the so-called nanometer-sized "hard (i.e. high glass-transition temperature, often crystallized) domains". The non-segregated hard segments and the soft segments form the so-called "soft (i.e. low glass-transition temperature, amorphous) matrix". Due to the presence of (hard domain + soft matrix) two-phase structure, polyurea is often referred to as being "segmented". Furthermore, since strong hydrogen bonding within the hard domains provides inter-molecular joining, polyureas are often referred to as being thermo-plastically cross-linked (in contrast to more commonly-observed covalently cross-linked) polymers. An example of a prototypical polyurea microstructure as revealed using the atomic force microscope (AFM) tapping mode is shown in Figure 1. Examination of this figure suggests that polyurea should be treated as a nano-composite (in which hard domains act not only as thermoplastic cross-links but also as rigid reinforcements within a continuous soft matrix) rather than a homologous amorphous material.

Due to their highly-complex internal microstructure described above, polyureas display a very broad range of mechanical responses under static and dynamic loading

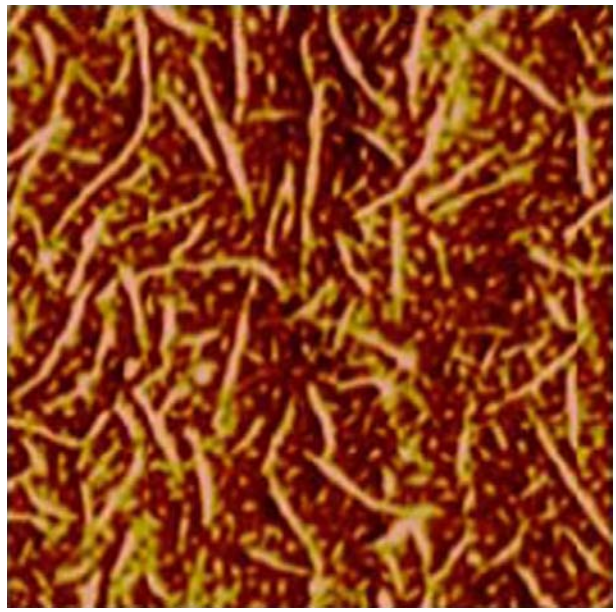

Source: Grujicic *et al*. (2010d)

Figure 1.
A typical tapping-mode AFM phase image of polyurea showing its micro-segregated structure consisting of ribbon-like hard domains and a soft matrix

conditions. The main features of these responses can be defined as (Grujicic *et al.*, 2011a, b; 2010b, f):

- a high-level of stress vs strain constitutive non-linearity;
- extreme strain-rate (and temperature) sensitivity; and
- a high degree of pressure dependence.

These types of mechanical responses have favored the use of polyurea as an abrasion/corrosion protection and blast/ballistic-impact mitigation material (Grujicic *et al.*, 2010c, d, e). For instance, polyureas are frequently used as:

- tough, abrasion-resistant, corrosion-resistant, durable and impact-resistant (epoxy/rubber replacement) spray-on coatings/liners in various construction/structural applications such as tunnels, bridges, roofs, parking decks, storage tanks, freight ships, truck beds, etc.;
- external and internal wall-sidings and foundation coatings for buildings aimed at minimizing the degree of structure fragmentation and, in turn, minimizing the extent of the associated collateral damage in the case of a bomb blast; and
- gun-fire/ballistic resistant and explosion/blast mitigating coatings/liners or inter-layers in blast-resistant sandwich panels for military vehicles and structures.

The applications mentioned above capitalize on the exceptional ability of polyureas to harden under applied loading and to alter/disperse shock-waves and absorb the kinetic energy associated with these waves/ballistic projectiles (under dynamic loading conditions) (Wallsten and Kosec, 2005; Taber *et al.*, 2006; Grujicic *et al.*, 2010f).

1.1 Traumatic brain injury

Due to the resulting high direct and indirect costs to society (through lost earning potential of the affected and the burden of care imposed on their families) and life-altering long-term consequences, TBI has become an important societal problem. TBI, among civilians is mostly caused by motor-vehicle accidents involving collision and rollover as well as by sport- and work-related accidents. On the other hand, TBI in military personnel is mainly the consequence of exposure to blast and ballistic impacts. In fact, TBI has become a signature injury of the on-going military conflicts. It should be noted that the increased occurrence of TBI in the military personnel is partly the result of the advances in the ballistic resistance of personnel protective armor/gear. That is, while the use of the advanced body armor and head protection gear have greatly reduced the rate of soldier fatality from explosion and ballistic attacks, the rate of TBI occurrence in the survivors has drastically increased (Wallsten and Kosec, 2005; Taber *et al.*, 2006; Okie, 2005). Among the various types of TBI observed in military personnel, of particular concern (with regard to diagnosis and treatment), are those associated with blast exposure which are not accompanied by visible, external, bodily injuries.

While impact-induced TBI associated with car crashes and sport/work-related accidents has been studied extensively for the last 20 years, blast-induced TBI has received comparable attention only over the last few years (Nyein *et al.*, 2010; Grujicic *et al.*, 2010a). It is, hence, not surprising that TBI causes (acceleration and impact of the head) in the former case are quite-well understood while similar understanding of blast-induced TBI has been lacking (Bhattacharjee, 2008; Warden, 2006).

TBIs experienced by the military personnel can be classified in a number of ways. According to the structural integrity of the skull upon blast/ballistic loading, TBIs can be classified as: penetrating (pTBIs) and closed (cTBIs) where the former involves skull penetration/fracture while, in the latter case, structural integrity of the skull is maintained. The present investigation deals with closed TBIs which could be further classified in different ways. According to the severity-level, closed TBIs can be classified as (Holm *et al.*, 2005):

- mild (mTBIs, also referred to as "concussions");
- moderate; and
- severe.

On the other hand, according to the origin of TBI-causing dynamic loading, closed TBIs can be classified as:

- primary TBI resulting from the propagation and reflection of shock-waves (within the intra-cranial cavity) produced directly by the blast;
- secondary TBI caused by the ballistic impact of a person's head with an object propelled by the blast; and
- tertiary TBI caused by the blast-induced propulsion of a person's head and its subsequent impact against a rigid/hard surrounding structure (Cernak *et al.*, 2001; Taber *et al.*, 2006).

The present work deals with mild, primary, closed TBIs.

The most frequently cited mechanisms responsible for the mild, primary, closed TBI are:

- compression of the thorax which causes a vascular surge into the brain (Cernak *et al.*, 2001);
- skull flexure which may create shock-waves within the brain;
- shock-wave ingress into the intra-cranial cavity through skull orifices; and
- bulk acceleration of the head (Grujicic *et al.*, 2010e).

In the present work, the last two TBI-inducing mechanisms are investigated.

1.2 Design of currently-used helmets

Helmet has been traditionally used as the main head protection gear in the military. However, the design of military helmets has continuously evolved in order to respond to ever-increasing lethality and diversity of threats, to take advantage of the new materials and fabrication/manufacturing technologies, and to meet continuously growing demands for lower weight and improved comfort. An overview of the evolution/advances in the helmet design from one used in the First World War to the ones currently in use can be found in Walsh *et al.* (2005). Currently, two helmet designs are mainly being used by the US military (Cernak *et al.*, 2001):

(1) the so-called advanced combat helmet (ACH); and

(2) the so-called light-weight marine corps helmet (LWH).

The present work deals with the ACH design (described below), while a fairly detailed description of the LWH design (not considered here) can be found in our recent work (Grujicic *et al.*, 2010d).

An ACH helmet consists of a 7.8-mm thick outer composite shell based on lower-content phenolic resin reinforced with higher-strength Kevlar® 129 fibers, a modified edge cut for lower protection surface and a "suspension system" (a set of discrete foam pads strategically placed on the interior surface of the helmet and held in place by Velcro-based hook-and-loop fasteners). A geometrical model of the ACH helmet, with all its basic components identified, is shown in Figure 2. To protect their intellectual property and maintain an advantage over their competitors, the helmet manufacturers have not revealed much detail regarding the material selection, fabrication methods and designs of the suspension pads. What is known for sure is that the suspension pads are made of an elastomeric foam-like material (e.g. ethylene vinyl acetate (EVA)) their geometrical dimensions and their locations in the helmet. A survey of the usage of foam-like materials carried out as part of the present work suggested that EVA foam is a good suspension-pad material candidate. Hence, EVA was used as the standard suspension-pad material in the present work.

1.3 Main objective

As mentioned earlier, the main objective of the present work is to assess the ability of polyurea, when used within the ACH (either as a suspension-pad material, composite-shell internal lining or composite-shell external coating), to mitigate the effects of blast loading and, in turn, to reduce the possibility of the occurrence/probability of mild, primary, closed TBI.

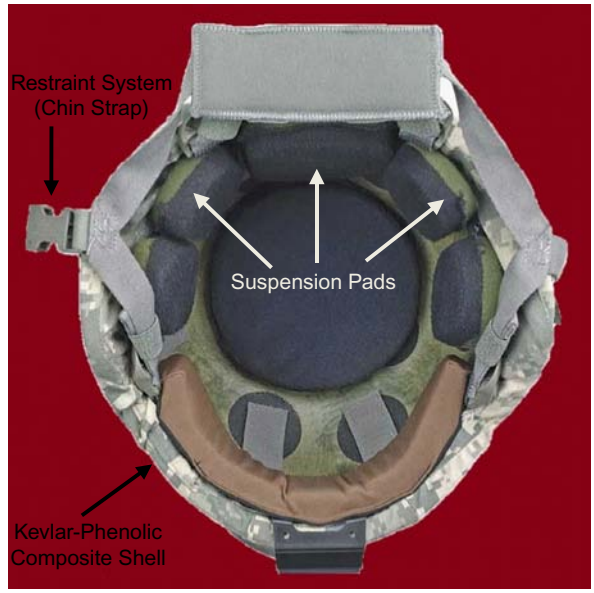

Source: Grujicic *et al*. (2010d)

Figure 2.
The ACH with its labeled main components: Kevlar-phenolic composite outer shell, interior suspensions pads and a restraint (chin strap) system

Organization of the paper

A brief description of a typical transient non-linear dynamics problem such as the one dealing with the interactions of an air-borne blast-wave with the unprotected and the protected human head is given in Section 2.1. Detailed descriptions of the geometrical and meshed models for the air/helmet/head assembly are presented in Section 2.2. A fairly detailed account of the material models assigned to air and the different sections of the helmet/head assembly is provided in Section 2.3. Formulation of the problem dealing with the interactions of an air-borne blast-wave with the helmet/head assembly is presented in Section 2.4. The details regarding the generation of a moving blast-wave within the air-filled portion of the computational domain are discussed in Section 2.5. The results obtained in the present work are presented and discussed in Section 3. The main conclusions resulting from the present work are summarized in Section 4.

2. Modeling and computational analysis

2.1 Blast-wave/solid-structure interaction analysis

Computational analysis of a typical transient non-linear dynamics problem, such as the interactions between an air-borne blast-wave with an unprotected or helmet-protected human head, involves geometrical/meshed modeling of the associated components/regions and, generally, the application of a numerical scheme to solve simultaneously the governing (mass conservation, linear momentum and energy conservation) equations along with the material constitutive equations and the equations defining the initial, boundary, contact and kinematic-constraint conditions. The governing equations mentioned above are typically discretized within a coupled

Eulerian/Lagrangian framework and solved using a second-order accurate explicit numerical scheme. Within this approach, the potential problems associated with large motions and deformations of the fluid (air, in the present case), are avoided by treating the fluid-filled region as an Eulerian (control-volume) region (within which the computational grid is fixed in space and time while the material(s) is allowed to move through it). On the other hand, the solid structure (the helmet/head assembly, in the present case), which experiences considerably less motion and deformation, is analyzed using a Lagrange scheme (the computational grid is tied to the material and moves and deforms with it).

All the transient non-linear dynamics calculations carried out in this work were done using a general purpose finite-element analysis software ABAQUS/Explicit (Dassault Systems, 2010). A detailed account of the key features of ABAQUS/Explicit relevant to the present study is provided in our recent work (Grujicic *et al.*, 2010a). Hence, only a very brief overview of this topic will be provided in the remainder of this section.

Interactions between the adjoining (non-adhering) components of the model are analyzed using the appropriate Lagrange-Lagrange and Euler-Lagrange contact algorithms. Likewise, adhesion between the remaining adjoining components of the model is accounted for using the appropriate kinematic constraints.

The Lagrange-Lagrange normal interactions are analyzed in ABAQUS/Explicit using a penalty-contact algorithm. Within this algorithm, (normal) penetration of the contacting surfaces is resisted by a set of linear springs which produce a contact pressure that is proportional to the depth of penetration. Typically, maximum default values, which still ensure computational stability are assigned to the (penalty) spring constants. Force equilibrium in a direction collinear with the contact-interface normal then causes the penetration to acquire an equilibrium (contact-pressure dependent) value. It should be noted that the no contact pressures are developed unless (and until) the nodes on the "slave surface" contact/penetrate the "master surface". On the other hand, the magnitude of the contact pressure that can be developed is unlimited. As far as the tangential Lagrange-Lagrange interactions (responsible for transmission of the shear stresses across the contact interface) are concerned, they are modeled using a modified coulomb-friction law. Within this law, the maximum value of the shear stresses that can be transmitted (before the contacting surfaces begin to slide) is defined by a product of the contact pressure and a static (before sliding) and a kinetic (during sliding) friction coefficient. In addition, to account for the potential occurrence of a sticking condition (sliding occurs by shear fracture of the softer material rather than by a relative motion at the contact interface), a maximum value of shear stress (equal to the shear strength of the softer material) that can be transmitted at any level of the contact pressure, is also specified.

Interactions between an Eulerian region (such as the one containing air and a propagating blast-wave) and a Lagrangian region (such as the one containing the helmet/head assembly) are analyzed using a fluid/solid contact algorithm. Within this algorithm, the outer surfaces of the solid structures define the interior boundaries for the Eulerian region. In general, the Eulerian and Lagrangian domains do not possess conformal meshes and, hence, the contact interfaces between the two could not be typically defined using mesh-based surfaces. In this case, contact interfaces between the Lagrangian and the Eulerian sub-domains are determined using the so-called "immersed boundary method" (Dassault Systems, 2010) which identifies, during each

computational time increment, the portion of the Eulerian sub-domain(s) which is occupied by the Lagrangian sub-domain(s). This ensures that the Lagrangian region, which resides, fully or partially within the Eulerian region(s) provides, no-flow boundary conditions to the Eulerian material in the direction normal to the local Eulerian/Lagrangian contact interface. At the same time, the Eulerian region provides normal and tangential loading forces to the Lagrangian region. As in the Lagrangian/Lagrangian interaction case, normal and shear stresses are transmitted across the Eulerian/Lagrangian interface in accordance with the aforementioned penalty and coulomb-law algorithms.

As far as the shear stresses are concerned they are transferred via a "slip/stick" algorithm. That is, shear stresses lower than the frictional shear stress are transferred without interface sliding, otherwise interface sliding takes place. The frictional shear stress is defined by a modified Coulomb law within which there is an upper limit to this quantity (set equal to the shear strength of the softer of the two materials).

In addition to the Eulerian-Lagrangian contacts, interactions (of a "sticky" character) also occur between different Eulerian materials. This type of interaction is a consequence of the kinematic constraint which requires that all Eulerian materials residing in a single Eulerian element are subjected to the same strain. The Eulerian-Eulerian contacts allow normal (tensile and compressive) stresses to be transferred between adjoining materials while no slip at the associated material boundaries is allowed.

2.2 Geometrical modeling and mesh pre-processing

The work presented in the present manuscript is a part of a larger-scale research project within which various blast mitigation approaches are investigated. Within this research effort, work is underway to analyze the interactions between a planar blast-wave and the whole human head, either unprotected or protected by a helmet. Examples of the typical pressure-field plots pertaining to the unprotected-head/air and protected-head/air assemblies are shown in Figure 3(a) and (b), respectively. For improved clarity, only one-half of the respective domains (obtained through the use of a coronal cut) are shown in these figures. The results obtained so far in this research project have been reported elsewhere (Grujicic *et al.*, 2010c, d) and the results currently being generated will be presented in one of our future communications.

Within the present work, whose main objective is the assessment of polyurea as a shock-mitigation material, a substantially simpler geometrical model (Figure 4), relative to the full head/helmet assembly shown in Figure 3(a) and (b), is utilized. The model used in the present work consists of a single square-base core sample running in the direction normal to the head. Six different configurations (cases) of the core sample are considered (Figure 4). In each case, the left most region is an Eulerian-type air-filled region. In Case A, the unprotected head case, there are four (skin/fat, skull, cerebro-spinal fluid (CSF), cerebrum) Lagrangian-type domains. In Case B, the skull region is removed in order to simulate the case of shock-ingress through skull orifices. Case C is the standard helmet-protected head case, which adds Kevlar®/Phenolic composite shell and EVA suspension-pad regions to the right of the air region. Cases D-F represent different modifications of Case C, through either replacement of the suspension-pad EVA material with polyurea (Case D) or addition of an internal (Case E) or external (Case F) coating to the composite shell. The following thicknesses were assigned to the different core-sample regions:

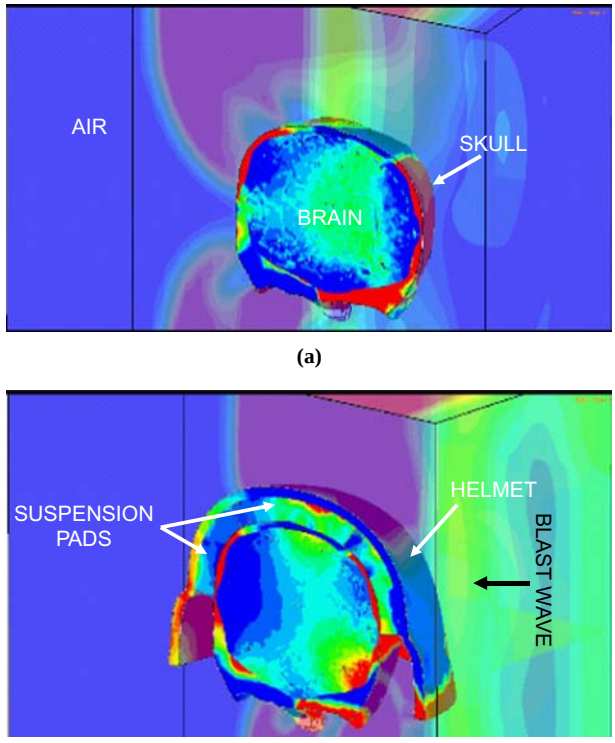

Figure 3.
Typical pressure-field plots pertaining to: (a) the unprotected-head/air; and (b) the helmet-protected head/air assemblies

Note: Only one-half of the model resulting from the use of a coronal cut is displayed

- air, 20 mm (assigned arbitrarily);
- Kevlar/Phenolic-resin composite helmet shell, 7.8 mm;
- external/internal polyurea coating, 2 mm (assigned arbitrarily);
- EVA/polyurea suspension-pad, 14 mm;
- skin/fat, 2 mm;
- skull, 6.5 mm;
- the CSF, 2 mm; and
- the cerebrum, 75 mm.

Thicknesses of the Lagrangian segments other than that for the polyurea coating, are chosen in such a way that they are consistent with the ACH helmet design or the average thicknesses of the skin, skull, the CSF and the cerebrum.

Interactions between air and the Kevlar/Phenolic-resin composite helmet shell are analyzed by defining the appropriate Eulerian/Lagrangian interface. As far as the interactions between the adjacent Lagrangian regions are concerned they are handled either using the Lagrange/Lagrange contact algorithm overviewed earlier (in the case

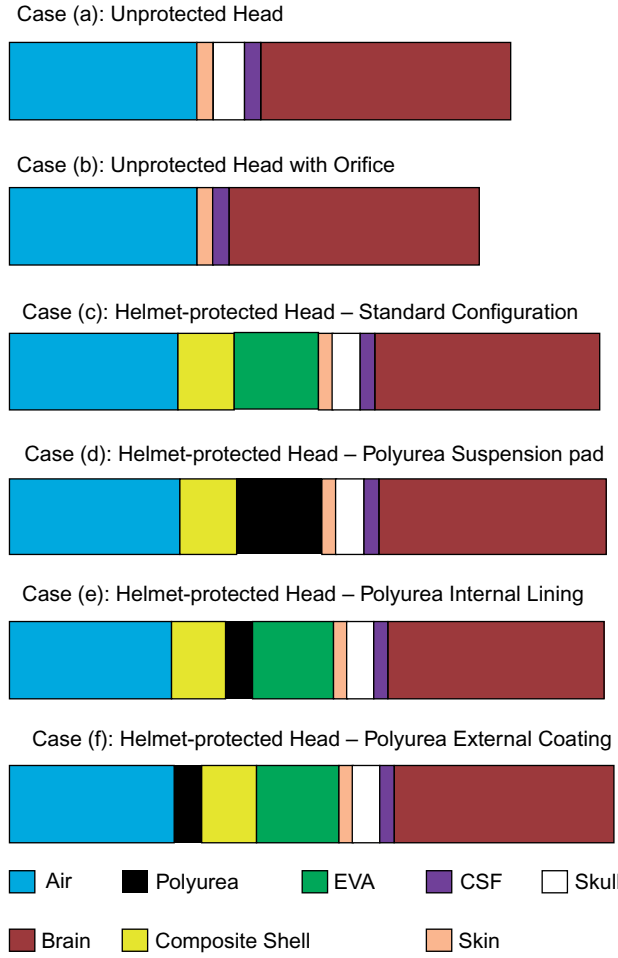

Figure 4.
Geometrical models (not drawn to scale) of various air/helmet/head configurations analyzed in the present work

of non-adhering adjacent Lagrangian regions) or through the use of tie-type kinematic constraints (in the case of adhering adjacent Lagrangian regions).

Meshing of Eulerian sub-domain. The air-filled sub-domain is discretized as a single column of non-distorting eight-noded "brick-shape" hexahedron Eulerian cells. To attain a balance between accuracy and computational efficiency, the average dimension of the Eulerian cells along the column axis is set to 0.01 mm. While the Eulerian mesh used is non-deformable, an adaptive meshing algorithm was employed in order to improve the resolution of the hydrodynamic fields in the regions at the propagating blast-wave front.

Meshing of the Lagrangian sub-domain(s). As mentioned earlier, there are up to seven Lagrangian segments, each filled with a different material. To enable an easy construction of various core sample cases by combining the attendant Lagrangian segments, each of the seven Lagrangian segments was meshed independently. Each of these segments is meshed using identical right-angled hexahedral solid elements with

a typical edge length of 0.01 mm. This mesh size was found to be a good compromise between accuracy and computational efficiency. The use of finer meshes was found to produce slightly different numerical values of the kinematic and mechanical field variables and material-state variables. However, the nature of the main findings obtained in the present work was not changed when finer meshes were used.

To account for the contacts and kinematic constraints that may exist between the adjacent Lagrangian segments, the following approach was utilized:

- in the case of non-adhering adjacent segments (composite-shell (or internal polyurea coating)/suspension-pad, suspension-pad/skin and skin/skull), the adjacent segments are allowed to establish a contact; and
- otherwise, in the case of adhering adjacent segments (external polyurea coating/composite-shell, composite-shell/internal polyurea coating, skull/CSF and CSF/cerebrum), tie-type kinematic constraints are imposed.

As mentioned earlier, complete definition of a transient non-linear dynamics problem requires specification of the appropriate mechanical models for all constituent materials. Hence, material models must be specified for all the aforementioned segments/sub-domain(s). A brief description of the mechanical models used to represent the response of these materials under blast-loading are presented in the next section.

2.3 Material models

The material (mechanical) models of interest here, define relationships between the field/material-state variables (pressure/stress, mass-density/specific volume, energy density, temperature, etc.). These relations are typically defined as:

- an equation of state;
- a strength model; and
- a failure model.

Partitioning of the material model in these three components is a natural consequence of the fact that, the total stress tensor can be represented as a sum of a hydrostatic stress (scales with negative pressure) tensor (which causes a change in the volume/density of the material) and a deviatoric stress tensor (which is responsible for the shape change of the material). The hydrostatic part of the stress is defined by the equation of state which specifies the corresponding functional relationship between pressure, mass-density, and internal-energy density/temperature. The deviatoric part of the stress, on the other hand, is defined by the strength model which specifies the appropriate functional relations between the deviatoric-stress components and various field quantities quantifying the extent and rate of material deformation as well as the effect of material temperature. A failure model, defines one or more stress-and/or strain-based conditions, which when attained, cause the material to fracture and lose its ability to support tensile normal and shear stresses. Due to the fact that blast levels considered in the present work typically do not cause any detectable damage to the helmet, skull or the inter-cranial brain matter and due to the (non-fracturable) fluid nature of air, failure of the materials encountered in the present problem was not considered. Furthermore, since blast loading scenarios considered in the present work are not generally associated with significant thermal-radiation effects or energy-dissipation induced heat effects (i.e. the shock

loading conditions fall into the weak-shock regime), the effect of temperature on the material response/behavior was not considered.

As discussed earlier, the present work deals with interactions between an air-borne blast-wave and (a core sample of) the helmet/head assembly. Since these interactions result in the formation of the shock-waves (in the case of the so-called "normal materials") or finite-amplitude spreading waves (in the case of the so-called "anomalous materials"), within the helmet/head assembly, special attention was paid to the ability of the material models used in the present work to enable formation of the blast/induced waves of the correct type. Specifically, as discussed in our prior work (Grujicic *et al.*, 2010d):

- shock-supporting normal materials must display material non-linearity of a type which yields an upward curvature in the associated pressure vs specific volume (reciprocal of the density) plot (i.e. pressure increases at a higher and higher rate as the specific volume decreases); and
- while the anomalous materials must possess a downward curvature in the associated pressure vs specific volume plot.

Air material model.

Equation of state. Air, which is used to fill the Eulerian sub-domain, is treated as an ideal gas and, consequently, its equation of state was defined by the ideal-gas gamma-law relation as (Davison, 2008):

$$P = -P_a + (\gamma - 1)\frac{\rho}{\rho_0}E \tag{1}$$

where P is the pressure (or more precisely overpressure relative to the ambient pressure, $P_a = 1\,\text{atm} = 101.3\,\text{Kpa}$), γ ($= 1.4$ for a diatomic gas like air the constant-pressure Cp to constant-volume $C_v = 717.6$ (J/Kg − k) specific heat ratio), ρ_0 ($= 1.225\,\text{kg/m}^3$) is the ambient-pressure (1 atm) air mass density, ρ is the current mass density and E is the volumetric energy density. Equation (1) is obtained from the standard form of the ideal-gas law through the use of the following two additional relations: $R = C_p - C_v$ and $E = C_v(T - T_o)/\rho_0$, where R is the air-specific gas constant while T and $T_o = 298\,\text{K}$ are, respectively, the current and the reference temperatures. Examination of equation (1) reveals that the total pressure $P + P_a$ scales linearly with ρ (i.e. with the reciprocal of the specific volume) and, hence, air behaves as a normal, shock-supporting material under (compressive) blast loading conditions.

Strength model. Since air is a gaseous material, it has no ability to support shear stresses and, hence, no strength model had to be defined for this material.

Kevlar/phenolic-resin composite material model.

Equation of state. In accordance with the work presented in Ansys Inc. (2007), Kevlar/phenolic-resin composite material is treated as an orthotropic material with material non-linearity's appearing in the hydrostatic (pressure-dependent) part of the stress tensor. Within the orthotropic equation of state used, pressure is defined as:

$$P = -K_1 e_{vol} + K_2 e_{vol}^2 - \frac{1}{3}(C_{11} + C_{21} + C_{31})e_{11}^d - \frac{1}{3}(C_{12} + C_{22} + C_{32})e_{22}^d - \frac{1}{3}(C_{13} + C_{23} + C_{33})e_{33}^d \tag{2}$$

where $K_1 = 1/9(C_{11} + C_{22} + C_{33} + 2(C_{12} + C_{23} + C_{31}))$ is the effective bulk modulus, e_{vol} (scales linearly with $(\rho_0/\rho) - 1$) is the volumetric strain, K_2, is a coefficient in the quadratic non-linear) correction to the P vs e_{vol}) and the last three terms on the right-hand side of equation (2) represent the contributions of the deviatoric strains, e^d_{ij}, to the pressure. It should be noted that a sum of these contributions is zero in the case of a isotropic linear elastic material.

It should be also noted that the presence of the $K_2 e^2_{vol}$ term in equation (2) introduces the material volumetric non-linearity. Since K_2 is greater than zero in the case of Kevlar/phenolic-resin composite, this material behaves as a normal shock-supporting material. Furthermore, due to an expected low extent of energy dissipation, no explicit dependence of pressure on the internal energy density is specified in equation (1). Values for all the parameters for the Kevlar/phenolic-resin composite equation of state can be found in our recent work (Ansys Inc., 2007).

Strength model. As far as the strength model is concerned, it is simply defined by a generalized Hooke's law which uses the orthotropic elastic stiffness matrix to map the deviatoric strain components to the corresponding deviatoric stress components. The components of the elastic stiffness matrix, C_{ij} appearing in equation (2) and in the equation for K_1, are defined in terms of the corresponding engineering constants E_{ij}, G_{ij} and v_{ij} ($i, j = 1, 2, 3$) using standard relations. Values for all the parameters for the Kevlar/Phenolic-resin composite strength model can be found in our recent work (Grujicic *et al.*, 2010d).

Polyurea material model.

Equation of state. To describe the mechanical response of polyurea under blast loading conditions, the material model reported in Amirkhizi *et al.* (2006) was used. Within this model, the hydrostatic response of the material is considered to be elastic while provisions are made for large deformations/motions of the material. Consequently, pressure is defined as:

$$P = -K(T)\frac{\ln(J)}{J}; \quad K(T) = K(T_{ref}) + m(T - T_{ref}) \tag{3}$$

where subscript *ref* is used to denote a quantity at the reference temperature, K is the bulk modulus, T is the temperature, m a material parameter and J (= det(F)) with the deformation gradient F being a quantity which maps the original/reference material configuration into the current/deformed material configuration and *det* denoting the determinant operator. Since $ln(J)$ represents the (logarithmic strain) volumetric strain and J decreases during compression, the effective bulk modulus $K(T)/J$ increases with an increase in volumetric compression. Thus, polyurea also behaves as a normal shock-supporting material. Values of all the parameters for the polyurea equation of state can be found in our recent work (Grujicic *et al.*, 2010d).

Strength model. Within the polyurea material model reported in Amirkhizi *et al.* (2006), deviatoric response of the material is assumed to be time-dependent and is treated using a geometrically-non-linear, materially-linear visco-elastic formulation. To account for the aforementioned time-dependent character of the material deviatoric response, evaluation of the deviatoric stress, σ', at the current time t has to take into consideration the entire deformation history of a given material point from the onset of loading at $t = 0$ to the current time. Based on the procedure outlined in Amirkhizi *et al.* (2006), σ' is defined as:

$$\sigma^{J}(t) = 2G_{\infty}\frac{T}{T_{ref}}\int_{0}^{t}\left(1+\sum_{i=1}^{n}p_i\exp\left(\frac{-(\xi(t)-\xi(\tau))}{q_i}\right)D'(\tau)\right)d\tau \tag{4}$$

where $G\infty$ is the "long-term" shear modulus (i.e. the value of the shear modulus after infinitely long relaxation time), n is the number of terms in the Prony series exponential-type relaxation function, pi and qi are, respectively, the amplitude and the relaxation time of each Prony series term, ξ is the so-called reduced time and D' is the deviatoric part of the rate-of-deformation tensor, D ($D'_{ij} = D_{ij} - 1/3{*}D_{ij}\delta_{ij}, i,j = 1,2,3$, δ_{ij} is the Kronecker delta second order tensor, summation is carried out over the repeated indices and trace denotes the trace operator). The reduced time is utilized in order to take into account the effect of temperature and pressure on the relaxation kinetics and is defined as:

$$\xi(t) = \int_{0}^{t}\frac{dt}{10^{A(T-C_{TP}P-T_{ref})/(B+T-C_{TP}P-T_{ref})}} \tag{5}$$

where A, B and C_{TP} are material constants. Through application of the reduced-time concept, the response of a material at temperature, T, and pressure, P, over a time period t is assumed to be identical to the response of the same material at the reference temperature and pressure over a time period $\xi(t)$. The rate-of-deformation tensor, D, is related to the deformation gradient, F, as:

$$D = sym(\dot{F}F^{-1}) \tag{6}$$

where "sym", the raised dot and superscript " -1", are used to denote, respectively, the symmetric part, the time derivative, and the inverse of a second order tensor. Values of all the parameters for polyurea strength model can be found in our recent work (Grujicic *et al.*, 2010d).

Skull material model.

Equation of state. Skull is composed of bone material which is characterized by relatively low value of the compressibility and an effectively-isotropic character of the material microstructure. Consequently, the hydrostatic part of the skull material model is represented using a Mie-Gruneisen equation of state with a zero value of the Gruneisen gamma parameter in the form:

$$P = \frac{\rho_0 C_0^2(1-(\rho_0/\rho))}{\left[1-s(1-(\rho_0/\rho))\right]^2} \tag{7}$$

where ρ_0 is the initial/reference density and coefficient C_0 (the sound speed) and s relates the shock speed U_s and the resulting particle velocity, U_p, as:

$$U_s = C_0 + s\cdot U_P \tag{8}$$

Equation (7) also referred to as a shock-Hugoniot equation of state, is often used to represent non-linear response (associated with an increase in bulk modulus) of the materials under a high level of compression. Thus, skull material also behaves as a normal, shock-supporting material. Values of all the parameters for the skull-material equation of state can be found in our recent work (Grujicic *et al.*, 2010d).

Strength model. Due to the high shear rigidity of skull material and an effectively-isotropic character of the material microstructure, the deviatoric response of the skull material is defined as being isotropic, linear elastic. Consequently, this response is completely quantified by a single material parameter, the shear modulus μ. The shear modulus is typically defined in terms of the corresponding Young's modulus E and the Poisson's ratio ν, as $\mu = E/[2(1 + \nu)]$. Values of all the parameters for the skull-material strength model can be found in our recent work (Grujicic *et al.*, 2010d).

CSF and cerebrum material models.

Equation of state. Following the analysis presented in our recent work (Grujicic *et al.*, 2010d), the materials constituting the CSF and cerebrum are assumed to be isotropic (direction-invariant) and homogeneous (spatially uniform) and to behave as elastic (time-invariant, materially-non-linear) materials with respect to their hydrostatic/volumetric response. In accordance with these assumptions/simplifications, the hydrostatic portion of the soft-tissue material model is defined using an initial value of the bulk modulus and one or more parameters defining the type and extent of non-linearity between the pressure, density, and internal energy density.

Specifically, following Moore *et al.* (2008), the non-linear hydrostatic/volumetric elastic response of the CSF and cerebrum materials is modeled using a Tait-type equation of state of the form:

$$P = B\left[\left(\frac{\rho}{\rho_0}\right)^{\Gamma_0+1} - 1\right] \tag{9}$$

where B and Γ_0 are material-specific parameters. It should be noted that the Tait-type equation of state is often used to model the behavior of fluids subjected to compressive (including the shock-based) loading. Since water is the dominant constituent of the CSF and cerebrum materials, and these materials were subjected to shock loading in the present work, the Tait-type equation of state was deemed an appropriate choice. Due to aforementioned chemical similarity between CSF/cerebrum materials and water, Parameters Γ_0 and B for the CSF and cerebrum materials are set equal to their counterparts in water. A summary of the Tait equation of state parameters ρ_0, B, and Γ_0 for the CSF and cerebrum materials can be found in our recent work (Grujicic *et al.*, 2010d).

Strength model. The deviatoric response of the CSF and cerebrum materials is generally considered as being time-dependent. However, as suggested by an analysis presented in our recent work (Grujicic *et al.*, 2010d), the relaxation times of these materials are at least two orders of magnitude longer than the characteristic times encountered in the present work. Hence, visco-elastic response of these materials is ignored and the materials are assumed to remain in a fully-unrelaxed state during a typical shock-loading event. Under these conditions, it appeared justified to treat the materials in question as time-invariant elastic materials. Furthermore, in order to account for potential effects associated with large-deformation/motion induced geometrical and material non-linearities, a hyper-elastic formulation had to be adopted for the deviatoric response of the materials in question.

Following the analysis carried out in our prior work (Grujicic *et al.*, 2010d), a Neo-Hookean hyper-elastic model was selected which defines the deviatoric stress as:

$$\sigma' = J^{-1} F \left[\mu \cdot \left(\log \sqrt{C} \right)^{dev} \right] F^T \tag{10}$$

where F and J were defined previously, μ is the shear modulus and $C = F^T F$ (is the right Cauchy-Green deformation tensor, and superscript T is used to denote a transpose operator). For simplicity, $\sqrt{C}$ term is replaced with its first-order and second-order linearized forms (Cuitiño and Ortiz, 1992). A summary of the Neo-Hookean hyper-elastic model parameters for CSF and cerebrum can be found in our recent work (Grujicic *et al.*, 2010d).

EVA foam material model. EVA foam material was modeled as a hyperelastic highly-compressible elastomeric-foam non-linear material whose behavior is described by the following strain energy function:

$$W = \sum_{i=1}^{N} \frac{2\mu_i}{\alpha_i^2} \left[\lambda_1^{\alpha_i} + \lambda_2^{\alpha_i} + \lambda_3^{\alpha_i} - 3 + \frac{1}{\beta_i} ((J)^{-\alpha_i \beta_i} - 1) \right] \tag{11}$$

where N represents the number of terms in the summation, μ_i, α_i, and β_i are material-dependent parameters, λ_i (i = 1, 2, 3) are the principal stretches (i.e. eigen values of the right (U) or the left stretch (V) tensors obtained through polar decomposition of the deformation gradient, F) defined as: $\lambda_1 = trace(U)$, $\lambda_2 = (1/2)[trace^2(U) - trace(U^2)]$ and $\lambda_3 = \det(U)$ and $J = \lambda_1 \lambda_2 \lambda_3 = det(F)$. In the present case, $N = 2.0$ was used. It should be noted that both terms on the right-hand side of equation (11) are affected by volumetric (J-dependent) effects, i.e. the deviatoric and volumetric terms are inter-dependent. This can be shown by casting equation (11) as:

$$W = \sum_{i=1}^{N} \frac{2\mu_i}{\alpha_i^2} \left[J^{-(1/3)\alpha_i} \left(\bar{\lambda}_1^{-\alpha_i} + \bar{\lambda}_2^{\alpha_i} + \bar{\lambda}_3^{\alpha_i} - 3 \right) + 3(J^{-(1/3)\alpha_i} - 1) + \frac{1}{\beta_i} ((J)^{-\alpha_i \beta_i} - 1) \right] \tag{12}$$

in which $\bar{\lambda}_i = J^{-(1/3)} \lambda_i$ and $\lambda_i (i = 1, 2, 3)$ are stretches associated with the deviatoric part of deformation alone. Stress (more precisely, the second Piola-Kirchhoff stress tensor, S) is obtained by differentiating the strain energy function U with respect to the right Cauchy-Green deformation tensor, $C (= 0.5(F^T F - I)$, I = second order identity tensor), as:

$$S = 2 \frac{\partial W}{\partial C} = 2 \frac{\partial W}{\partial \lambda_k} \frac{\partial \lambda_k}{\partial C} \tag{13}$$

The term $(\partial W / \partial \lambda_k)$ is obtained by properly differentiating equation (11), the second term is defined by the well-known relations between the eigen values and the components of a second order tensor while summation over repeated indices is implied in equation (13). The (true) Cauchy stress, σ, can then be computed from the corresponding second Piola-Kirchoff stress, S, using the following relation:

$$\sigma = J^{-1} F S F^T \tag{14}$$

Since EVA foam becomes volumetrically stiffer as it is compressed, this material behaves as a normal shock-supporting material. A summary of the EVA foam material model parameters can be found in our recent work (Grujicic *et al.*, 2010d).

Equation of state. The EVA-foam material model presented above defines the complete stress tensor. Hence, it is not necessary to partition this stress into its hydrostatic and deviatoric components. However, in cases in which the commercial software expects separate definitions of the EOS and the strength model, one can readily derive a hydrostatic-stress function (and, in turn, pressure) from the total-stress function.

Strength model. If required, the deviatoric stress can be defined as a difference between the total stress and the hydrostatic stress.

Skin/fat-tissue material model. The skin (as well as the companion muscle tissue) is treated as a single material and modeled using a Mooney-Rivlin hyperelastic isotropic material model which is defined by the following strain energy function:

$$W = A_1(I_1 - 3) + A_2(I_2 - 3) + A_3\left(I_3^{-2} - 1\right) + A_4(I_3 - 1)^2 \tag{15}$$

In equation (15), the material-dependent parameters A_3 and A_4 are related to the other two parameters, A_1 and A_2, as:

$$A_3 = \frac{1}{2}A_1 + A_2 \tag{16}$$

and:

$$A_4 = \frac{A_1(5\nu - 2) + A_2(11\nu - 5)}{2(1 - 2\nu)} \tag{17}$$

To obtain the components of the Cauchy stress, an analogous procedure to that described in the EVA foam material model case is used. Since skin/fat material becomes volumetrically stiffer as it is compressed, this material also behaves as a normal shock-supporting material. A summary of the skin/fat material model parameters can be found in our prior work (Grujicic *et al.*, 2009).

Equation of state. As in the EVA-foam material model case presented above, when required, a hydrostatic-stress function (and, in turn, pressure) can be derived from the total-stress function obtained using the procedure described above.

Strength model. If required, the deviatoric stress can be defined as a difference between the total stress and the hydrostatic stress.

2.4 Problem formulation

As mentioned earlier, the problem analyzed in the present work deals with the interaction of an air-borne blast-wave with a core sample of the head or a helmet/head assembly. As seen in Figure 4, the computational domain contains an air-filled Eulerian sub-domain. The initial pressure in this sub-domain is set to the atmospheric level and no-flow boundary conditions are applied to the four lateral faces of the sub-domain. On the front face of this sub-domain (the far left side of this domain in Figure 4), a time-dependent pressure boundary condition (details presented in next section) is applied. As a result, a blast-wave enters this sub-domain and propagates towards the head/helmet external surface. Upon reflection of the blast-wave from this surface, the reflected wave propagates in the opposite direction and ultimately exits the Eulerian sub-domain.

All the Lagrangian segments present in a given configuration are assumed to be initially stationary and stress-free. Since the Lagrangian sub-domain used represents

a square-base core sample (cut-out) through the helmet/head assembly in a direction normal to the helmet outer surface, zero displacement/velocity boundary conditions are applied along all the four lateral faces of this domain. The back face of the cerebrum was either fixed in the column-axis direction or set free. The choice of this boundary condition was found not to affect the main conclusions resulting from the present work.

2.5 Blast-wave loading

As mentioned in the previous section, blast loading conditions used in the present study were obtained by prescribing the appropriate pressure history (consistent with explosive-charge detonation in free-air) to the front-face of the Eulerian region. In our previous work (Grujicic *et al.*, 2010a, c, d), 5.2 and 18.6 atm peak overpressures were used. It is currently believed that these pressure levels are responsible for more severe TBI cases and that peak overpressures around 1 atm should be investigated in the case of mTBIs. To understand the nature of time-dependent pressure boundary condition used in the present work, a brief description of explosion-induced blast-shock generation in air is described below.

Detonation of an explosive charge in free-air or on the ground converts, at a very high rate, the solid explosive into a highly-compressed, rapidly-expanding detonation-product gaseous mass. Interactions of the rapidly expanding gaseous detonation products with the surrounding air produce outward-propagating air-borne shock-waves. These shocks are of a spherical geometry in the case of free-air explosion and of a hemispherical character in the case of ground-level explosion. In contrast to the (smooth/continuous) sound/acoustic waves, shock-waves are characterized by discontinuities in pressure, density, etc. across the wave front. A typical plot of the pressure history at a fixed point relative to the free-air explosive-detonation location is shown in Figure 5. It is seen that the arrival of the shock-wave to the point in question

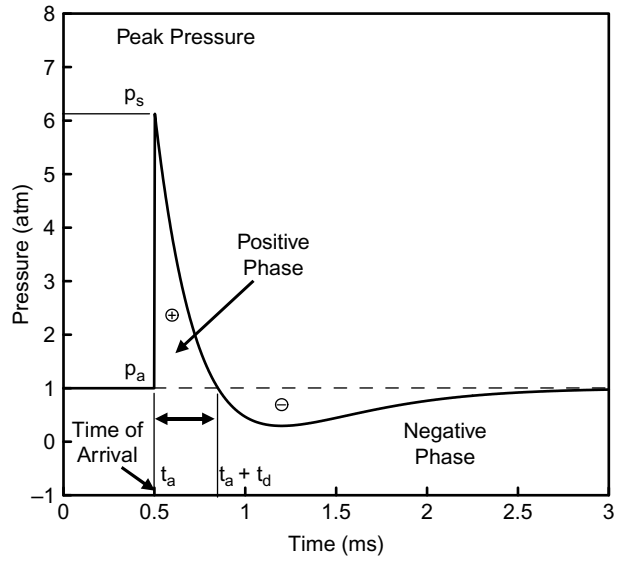

Figure 5.
A typical free-air pressure vs time relation at a fixed point as defined by the biphasic Friendlander equation

(at the post-detonation time, t_a), produces an abrupt change in pressure (from its initial/ambient value, P_a, to a peak value, P_s; $P_s - P_a$ is generally referred to as the peak overpressure). Subsequently, the pressure decreases and, at a post-detonation time of t_d (typically $t_d - t_a$ is referred to as the positive phase duration and is on the order of a few tens of microseconds) becomes equal to the ambient pressure, P_a. Thereafter, within the so-called suction-phase, the pressure first continues to drop, then levels off and finally begins to recover towards the ambient pressure level.

The pressure vs time relation shown in Figure 5 is typically described using the biphasic Friendlander equation of the form:

$$P(t) = (P_s - P_a)e^{-(t-t_a)/\tau}\left[1 - \frac{t - t_a}{t_d}\right] + P_a \tag{18}$$

where τ is a time-based decay constant which controls both the rate of the initial decrease of pressure and its farthest negative departure from the ambient pressure. It should be noted that blast-induced overpressure, $P(t) - P_a$, has two components:

(1) incident pressure, P_i; and

(2) reflected pressure, P_r.

The two components of the pressure are defined by the respective functional relations in accordance with equation (18). Parameters t_a and t_d are identical for the two components of pressure while the remaining two parameters P_s and τ generally differ in the two cases. The total blast-induced pressure acting on a small section of a (loaded) surface whose outward normal makes an angle θ with a vector connecting the surface section to the explosive charge centroid is given by:

$$P(t) = P_i(t)[1 + \cos\theta - 2\cos^2\theta] + P_r(t)\cos^2\theta, \cos\theta > 0 \tag{19a}$$

$$P(t) = P_i(t), \quad \cos\theta \leq 0 \tag{19b}$$

Examination of equation (19a) reveals that in the case of a surface which is tangential to the spherically expanding blast-wave ($\cos\theta = 1$), only the reflected component of the pressure is present. In contrast, in the case of a surface that is along one of the radial directions ($\cos\theta = 0$), only the incident/side-on pressure component is present. In the present case, the ("loaded") surface (Eulerian-domian front face) represents a section of the expanding air-borne blast-wave front, rather than an impacted surface. Hence, only the incident component of pressure is used to define the boundary conditions on the Eulerian-domian front face.

It should be noted that the boundary conditions in question are applied to the front face of the air-filled Eulerian region and not to the outer surface of the Lagrangian region. Loading of the outer surface of the Lagrangian domain is the result of the impingement of the air-borne blast-wave onto this surface. When such blast-wave strikes the outer surface of the Lagrangian domain, it gets reflected (i.e. the air molecules are forced to move in the direction opposite to the incident direction). Due to conservation of the linear momentum, the peak overpressure associated with the resulting shock-wave within the target structure is increased relative to that of the incident blast-wave. This magnification, which can be highly non-linear, depends on the strength of the incident blast-wave and the angle of incidence. For weak

shock-waves, a peak overpressure magnification factor of 2.0 is typically obtained. Amplification factors as high as eight are found in the case of an ideal gas and as high as 20 in the case of real gases (in which molecule dissociation and ionization may occur) (Cooper, 1996).

3. Results and discussion

3.1 Determination of the blast-wave induced pressure vs time histories

As mentioned earlier, peak overpressure around 1 atm (or lower) are of interest when dealing with mTBIs. Figure 6(a) shows pressure vs time traces experimentally determined in the present work. The experimental set-up involved the detonation of a free-air suspended explosive charge, 0.0568 kg of Pentolite with a TNT pressure equivalence of 1.42, and an array of (side-on oriented) pressure gauges placed at different radial/stand-off distances from the explosive charge. The results shown in Figure 6(a) pertain to five different stand-off distances of 1.067 m (3.5 ft), 1.22 m (4 ft), 1.83 m (6 ft), 2.44 m (8 ft) and 3.05 m (10 ft).

The results shown in Figure 6(a) are fitted to the biphasic Friendlander equation, equation (18), using the conventional least-squares method. The resulting four biphasic Friendlander equation parameters for the incident component of pressure, as a function of the stand-off distance are plotted in Figure 7(a)-(d).

In the absence of experimentally measured pressure vs time traces, these relations are often predicted using CONWEP, an empirically-based blast simulation code developed by the US Army Corps of Engineers (Hyde, 1988). Within the CONWEP model (Hyde, 1988), all the incident and reflected pressure parameters used in equation (18) are functions of a scaled distance, (defined as a ratio of (i) the distance between the loaded surface and the explosive charge centroid; and (ii) a cube root of the TNT-equivalent explosive-charge mass). Thus, to obtain a complete pressure history at a loaded surface, one needs to specify:

- TNT-equivalent explosive-charge mass;
- the distance from the loaded surface and the explosive-charge centroid; and
- the orientation of the loaded surface relative to the explosive charge centroid.

Application of the CONWEP model under the conditions defined in connection with Figure 6(a) produced the corresponding pressure vs time traces shown in Figure 6(b).

A comparison of the results shown in Figure 6(a) and (b) reveals that pressure vs time traces predicted by the CONWEP model are in reasonably good agreement with their experimental counterparts. Since the experimental results are believed to be inherently more accurate than their CONWEP counterparts, they were primarily used in the present work. In few additional analyses in which CONWEP-model based pressure vs time traces were used, qualitatively comparable but quantitatively different results were obtained. However, the basic conclusions resulting from the present work were not changed by the choice (experimental vs CONWEP-model based pressure loading conditions).

3.2 Intra-cranial stress and particle velocity histories

While experimentally-determined pressure vs time traces associated with all five stand-off distances, Figure 6(a), were utilized in the present work, only the results associated with the 1.067 m (3.5 ft) stand-off distance are presented. The results which are not shown are

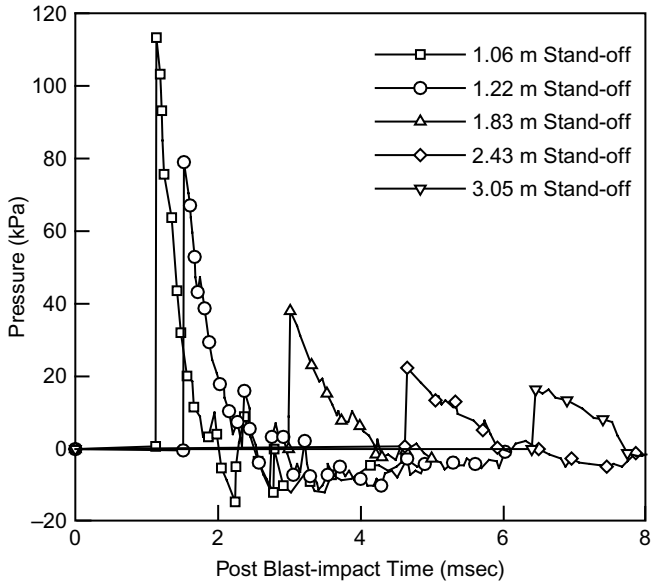

(a)

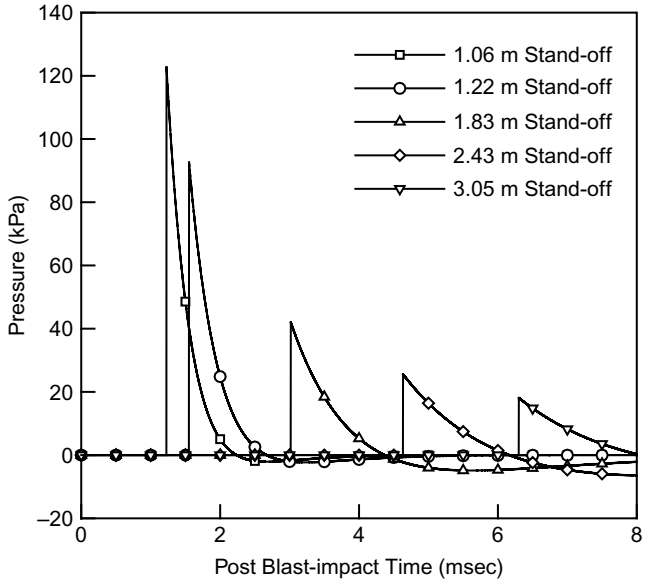

(b)

Source: Hyde (1988)

Figure 6.
(a) Experimentally-determined variation of pressure with time at five stand-off distances associated with free-field detonation of 0.0568 kg of Pentolite; and (b) the corresponding computed pressure vs time traces obtained using the CONWEP model

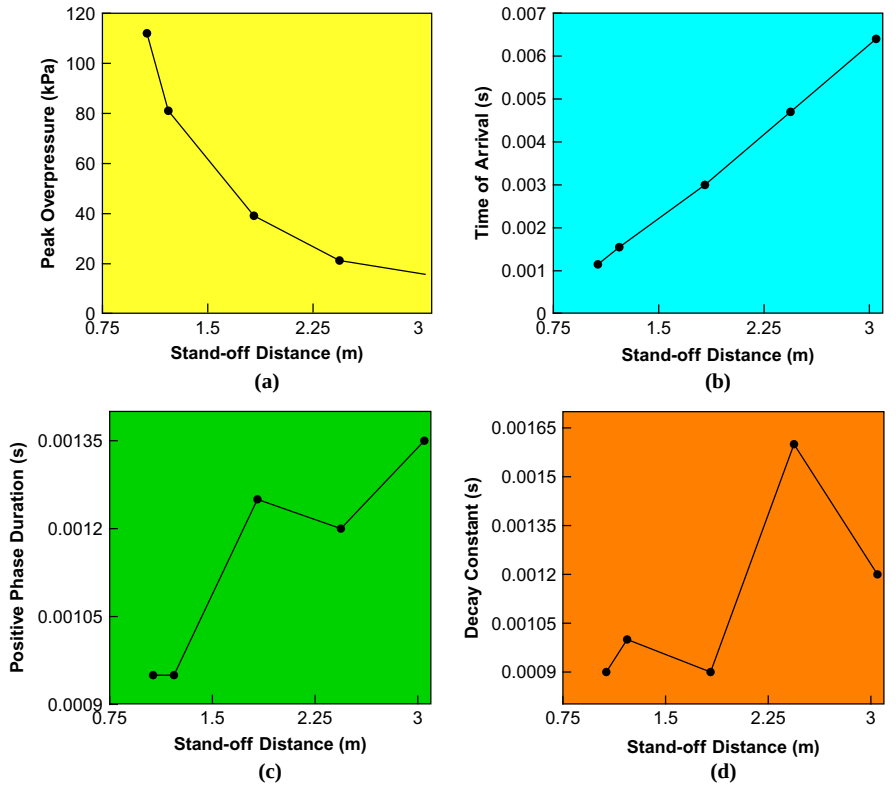

Figure 7.
Variation of the bi-phasic Friendlander function parameters with the stand-off distance for the case of free-field detonation of 0.0568 kg of Pentolite: (a) ps; (b) ta; (c) td; and (d) τ

quantitatively different but qualitatively similar so that the basic conclusions could be drawn using the 1.067 m (3.5 ft) stand-off distance based results alone.

Case A: unprotected head. The temporal evolution of axial (normal) stress at two brain locations at distances of 5 and 70 mm from the CSF/cerebrum interface, respectively, in the unprotected head case is shown in Figure 8(a). The corresponding results but for the particle velocity are shown, respectively, in Figure 8(b).

Examination of the results shown in Figure 8(a) and (b) reveals that:

- The shock-wave arrives at the locations 1 and 2 at post blast-impact times of 78 and 120 ms, respectively.
- The peak compressive axial stress at location 1 is ca. 1.3 MPa and that location 2 is around ca. 1.55 MPa. These values are about an order of magnitude higher than the blast-wave peak overpressure (ca. 0.117 MPa), Figure 6(a). This finding reconfirms the concept of (non-linear) blast-wave load amplification.
- Since the end of the cerebrum region was left free, reflection of the incident shock from the cerebrum-end free-surface causes the formation of a tensile (more precisely a release) wave with a peak (positive, tensile) axial stress of ca. 1.1 MPa. In our previous work (Grujicic *et al.*, 2010c), it was shown that within the intra-cranial cavity, tensile-stress regions develop as a result of the interaction/

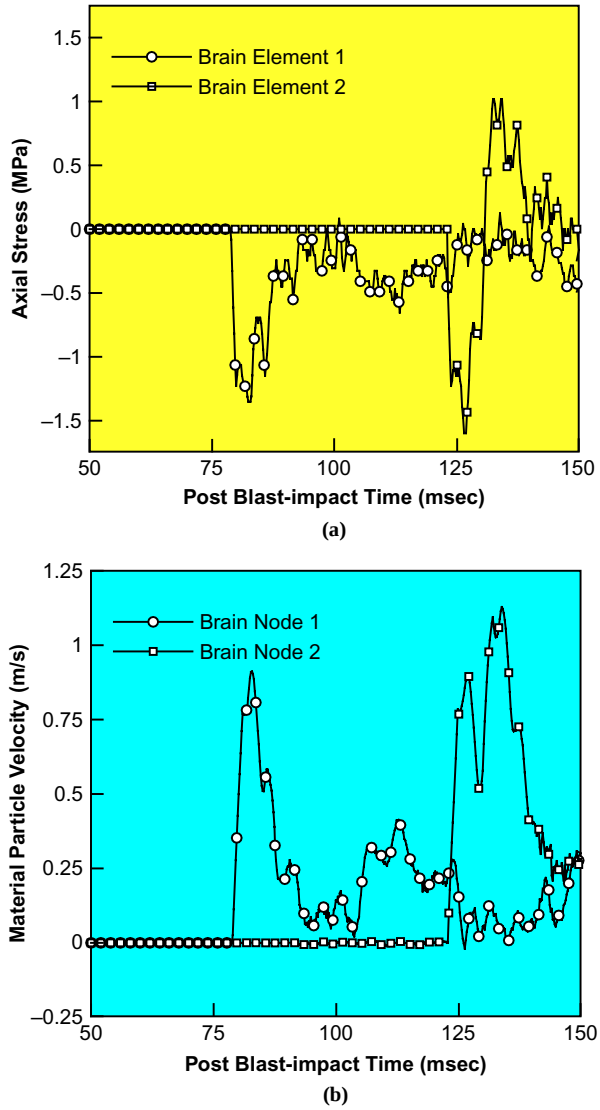

Notes: Analysis conditions: (i) explosive charge: Pentolite; (ii) charge mass: 0.0568 kg; TNT pressure equivalence: 1.42; (iv) stand-off distance: 1.067m (3.5 ft); and (v) core sample configuration: Case A

Figure 8.
Temporal evolution of (a) the axial stress; and (b) particle axial velocity at distances of 5 mm (location 1) and 70 mm (location 2) from the CSF/cerebrum interface, respectively

intersection of various shock and release waves and that the magnitude of these tensile stresses can be correlated with the (free-surface) release wave peak stress. Hence, even though the cerebrum free end is a non-physical entity, it is used in the present work for its practicality.

- Particle velocities at the two brain locations are mutually compatible (ca. 0.85 m/s) and increase, as expected, to about 1.15 m/s after reflection from the cerebrum free end.

Case B: unprotected head with orifice. The results analogous to the ones shown in Figure 8(a) and (b) but for the case of shock-wave ingress through a skull orifice into the intra-cranial cavity are shown in Figure 9(a) and (b).

Examination of the results shown in Figure 9(a) and (b) and their comparison with the corresponding results shown in Figure 8(a) and (b) reveals that:

- The time of arrival of the shock-wave to the two previously-defined brain locations is shorter by about 15-20 μs. This finding is expected considering the fact that the total shock travel distance is reduced in the present case by the thickness of the skull domain.
- Both the compressive axial stress at location 1 and the compressive and tensile stresses at location 2 are larger in magnitude than their Case A counterparts.
- As far as the particle velocities in the core sample configurations A and C are concerned, they are comparable for the incident shock and higher, for the reflected wave in Case C. These findings clearly show that blast-wave ingress into the intra-cranial cavity through the skull orifices creates a higher probability for the occurrence of mTBI.

Case C: helmet-protected head – standard configuration. The corresponding results for the case of the head protected with a helmet in the standard configuration are shown in Figure 10(a) and (b).

Examination of the results shown in Figure 10(a) and (b) and their comparison with the corresponding Case A results shown in Figure 8(a) and (b) reveals that:

- The times of arrival of the shock-wave to the two previously-defined brain locations are longer by a factor of four relative to those obtained in Case A. This finding is expected considering the fact that the total shock travel distance is increased by ca. 22 mm due to the presence of the helmet shell and the suspension pad layers and due to the low-density foamy character (resulting in low shock speeds) of EVA.
- Both the incident (compressive) and reflected (tensile) peak axial stresses are lowered by ca. 50 percent in comparison to their Case A counterparts.
- The accompanied particle-velocity peak-value reductions are about 35 percent. These findings clearly demonstrate the blast impact protection capability offered by the standard configuration of the combat helmet.

Case D: helmet-protected head – polyurea suspension pad. The corresponding results for the case of the head protected with a helmet equipped with polyurea suspension pads are shown in Figure 11(a) and (b).

Examination of the results shown in Figure 11(a) and (b) and their comparison with the corresponding Case A results shown in Figure 8(a) and (b) and Case C results shown in Figure 10(a) and (b) reveals that:

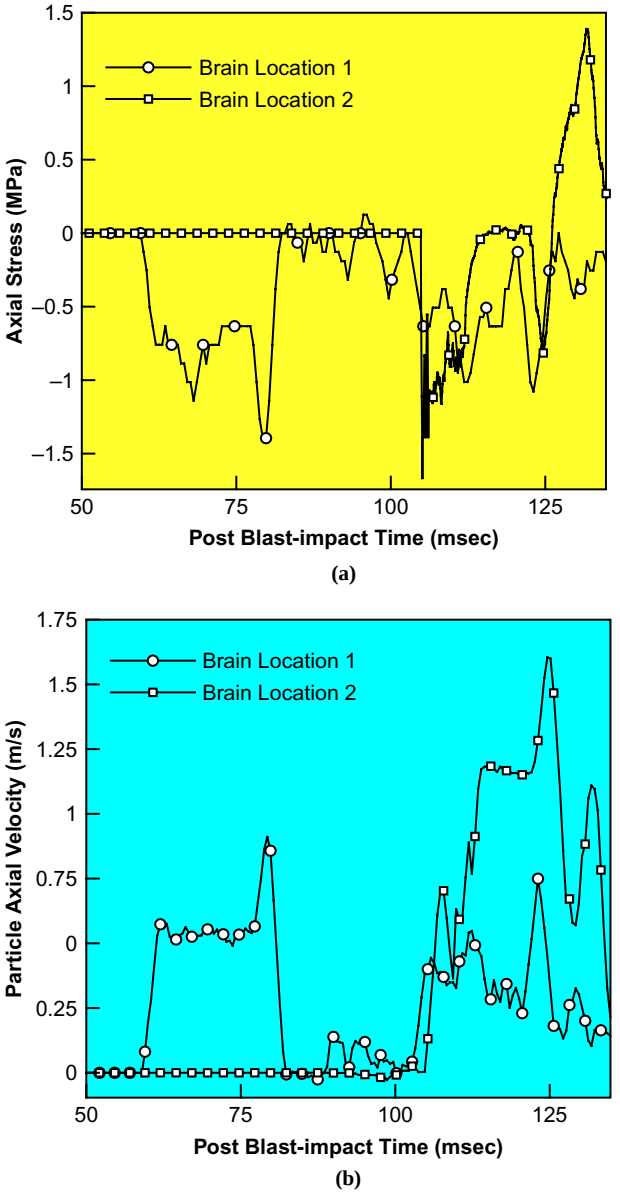

Notes: Analysis conditions: (i) explosive charge: Pentolite; (ii) charge mass: 0.0568 kg; TNT pressure equivalence: 1.42; (iv) stand-off distance: 1.067m (3.5 ft); and (v) core sample configuration: Case B

Figure 9.
Temporal evolution of (a) the axial stress; and (b) particle axial velocity at distances of 5 mm (location 1) and 70 mm (location 2) from the CSF/cerebrum interface, respectively

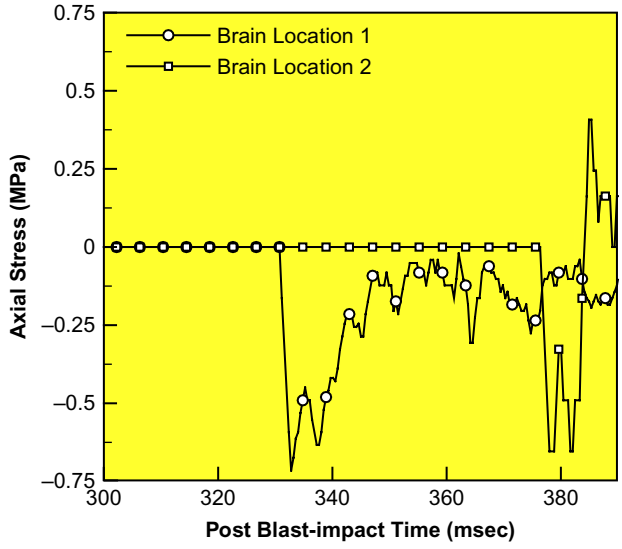

(a)

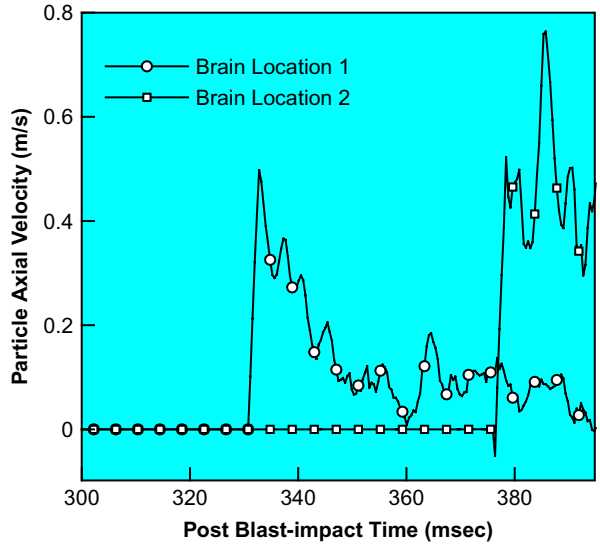

(b)

Figure 10.
Temporal evolution of (a) the axial stress; and (b) particle axial velocity at distances of 5 mm (location 1) and 70 mm (location 2) from the CSF/cerebrum interface, respectively

Notes: Analysis conditions: (i) explosive charge: Pentolite; (ii) charge mass: 0.0568 kg; TNT pressure equivalence: 1.42; (iv) stand-off distance: 1.067 m (3.5 ft); and (v) core sample configuration: Case C

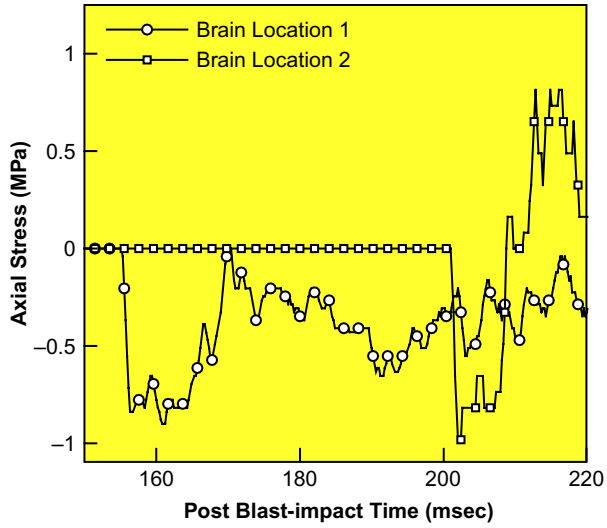

(a)

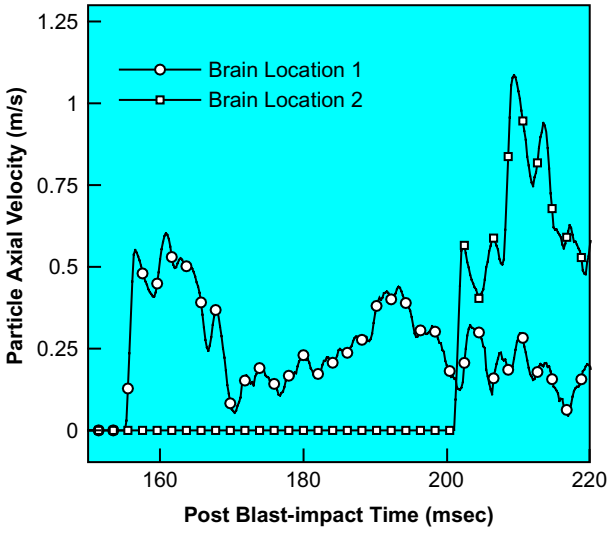

(b)

Notes: Analysis conditions: (i) explosive charge: Pentolite; (ii) charge mass: 0.0568 kg; TNT pressure equivalence: 1.42; (iv) stand-off distance: 1.067 m (3.5 ft); and (v) core sample configuration: Case D

Figure 11.
Temporal evolution of (a) the axial stress; and (b) particle axial velocity at distances of 5 mm (location 1) and 70 mm (location 2) from the CSF/cerebrum interface, respectively

- Since both the axial stress and axial particle-velocity peak values are reduced in the present case relative to the Case A, the helmet in the present configuration still provides a level of protection against blast impact loading.
- Since both the axial stress and axial particle-velocity peak values are increased in the present case relative to the Case C, the introduction of polyurea suspension pads appears to compromise blast impact protection capability of the combat helmet. This finding should be compared with the findings obtained in our recent work (Grujicic *et al.*, 2010c) which showed that at 18.2 atm blast peak pressure polyurea suspension pads clearly outperform their EVA counterparts while, at a blast peak pressure of 5.2 atm, the blast protection efficacies of the two types of suspension pad materials was comparable. The present results show that as the blast peak pressure is further reduced, EVA begins to outperform polyurea. As discussed in our previous work (Grujicic *et al.*, 2010c), the improved performance of EVA at lower blast peak pressures is related to the structure (single-wave front/highly-diffuse at low pressure vs two-wave/high-gradient at high pressures) of the shock-wave front.

Case E: helmet-protected head – polyurea internal lining. The corresponding results for the case of the head protected with a helmet equipped with EVA suspension pads and a polyurea internal lining are shown in Figure 12(a) and (b).

Examination of the results shown in Figure 12(a) and (b) and their comparison with the Case C results shown in Figure 10(a) and (b) reveals that the presence of a 2-mm thick polyurea internal lining reduces the intra-cranial stresses and particle velocities by ca. 5 percent and 10-15 percent, respectively. This finding clearly shows that the presence of such a lining is beneficial from the standpoint of reducing the potential for mTBI (although the overall shock mitigation capability improvement is relatively small). It is anticipated that through the use of an optimization procedure one can determine the mass-weighted optimal thickness of this lining in order to maximize the blast protection performance of the ACH.

Case F: helmet-protected head – polyurea external coating. The corresponding results for the case of the head protected with a helmet equipped with EVA suspension pads and a polyurea external coating are shown in Figure 13(a) and (b).

Examination of the results shown in Figure 13(a) and (b) and their comparison with the Case C results shown in Figure 10(a) and (b) reveals that the presence of a 2-mm thick polyurea external coating degrades the blast protection efficacy of the combat standard-configuration helmet. These results are consistent with the ones obtained by Amini *et al.* (2010), in their direct impact-induced pressure-pulse experiments. The results reported in Amini *et al.* (2007) were rationalized as being the consequence of an increased transfer of the blast load to the polyurea coated substrate due to improved impedance matching.

It should be noted that despite the fact that the present results suggest that use of polyurea in different components of the ACH does not significantly improve the blast mitigation potential of this helmet, one should recognize the fact that this finding was obtained only for a specific formulation of polyurea (Amirkhizi *et al.*, 2006). In our on-going research, it is found that the mechanical response of polyurea is greatly affected by even relatively small changes in its chemical make-up as well as in its synthesis route. Hence, one cannot rule out the possibility that polyureas (with different formulations than the one used here) may have a positive effect on the blast-protection capability of the ACH.

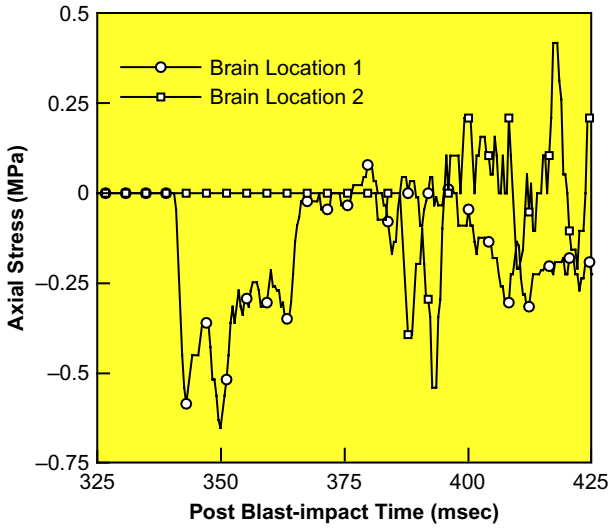

(a)

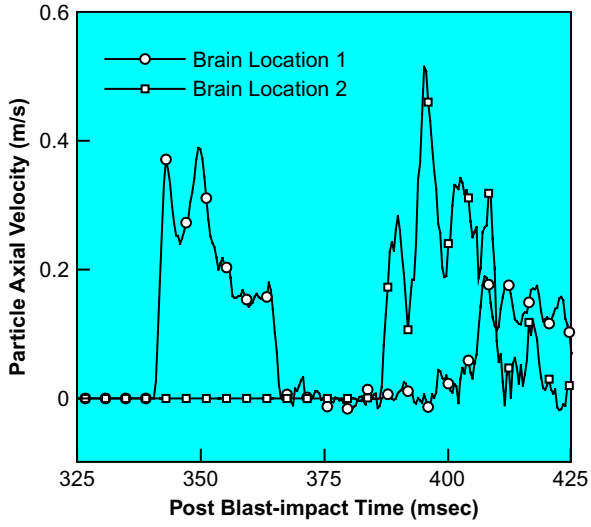

(b)

Notes: Analysis conditions: (i) explosive charge: Pentolite; (ii) charge mass: 0.0568 kg; TNT pressure equivalence: 1.42; (iv) stand-off distance: 1.067 m (3.5 ft); and (v) core sample configuration: Case E

Figure 12.
Temporal evolution of (a) the axial stress; and (b) particle axial velocity at distances of 5 mm (location 1) and 70 mm (location 2) from the CSF/cerebrum interface, respectively

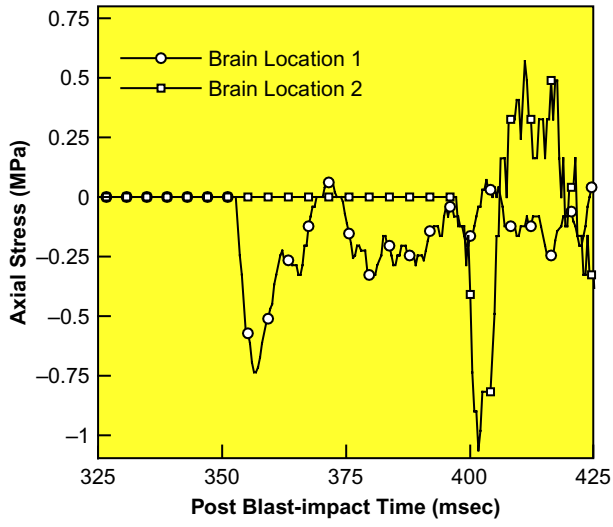

(a)

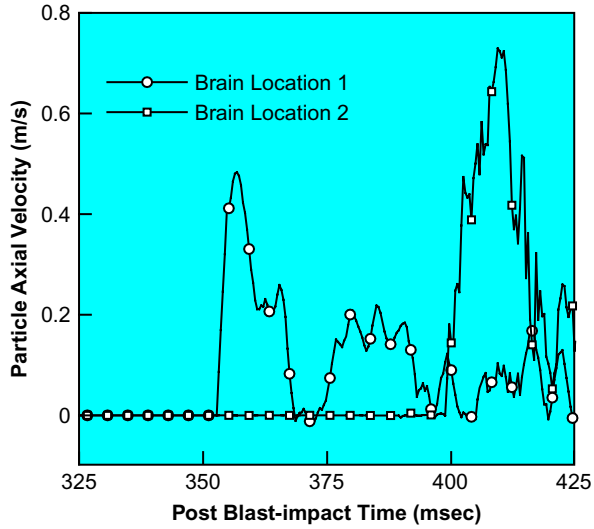

(b)

Figure 13.
Temporal evolution of (a) the axial stress; and (b) particle axial velocity at distances of 5 mm (location 1) and 70 mm (location 2) from the CSF/cerebrum interface, respectively

Notes: Analysis conditions: (i) explosive charge: Pentolite; (ii) charge mass: 0.0568 kg; TNT pressure equivalence: 1.42; (iv) stand-off distance: 1.067 m (3.5 ft); and (v) core sample configuration: Case F

3.3 Brief discussion

The results presented in the previous section reveal that among different polyurea-based modifications of the ACH, only the one associated with the use of a 2-mm thick polyurea internal lining yields an improvement in the helmet blast protection performance. Since all the constituent materials analyzed in the present work support shock formation under compressive loading (i.e. they all act as "normal" materials) it is interesting to establish if this finding could have been predicted using the so-called "impedance-matching" technique (Grujicic *et al.*, 2010d). To apply this technique one must first obtain the (compressive) axial stress vs particle velocity Hugoniot relations. To obtain these relations, a separate set of finite element analyses was carried out in which a single-material parallelepiped shaped slug (subjected to zero lateral-strain boundary conditions) impacts (at a zero obliquity angle) a rigid wall. More details regarding this type of finite element analyses can be found in our recent work (Grujicic *et al.*, 2010b). Slug-rigid wall collision results in:

- the formation of a (compressive) shock propagating in the (axial) direction opposite to the slug motion direction; and
- a zero particle-velocity region behind the shock.

By determining the shock speed for a given slug incident velocity, the shock-speed vs particle velocity Hugoniot relation can be established for the slug material. By combining this relation with the shock jump equations the needed axial stress vs particle velocity Hugoniot relations can be obtained.

The resulting shock-speed vs particle axial velocity and the negative axial-stress vs particle axial velocity Hugoniot relations, for the seven Lagrangian-domain materials obtained using the aforementioned procedure, are shown in Figure 14(a) and (b), respectively. It should be observed that, for improved clarity, log-log plots were used in these figures.

Since a detailed impedance-matching technique will be presented in our future work, only an example of the results obtained using this analysis will be presented in the remainder of this section. Specifically, the results associated with the helmet altered using a polyurea internal lining, Case E, obtained using the impedance-matching technique are shown in Figure 15. In Figure 15, the initial air-borne blast-wave is represented by point *A* (not shown in Figure 15, for improved clarity). In accordance with the impedance-matching technique (Grujicic *et al.*, 2010d), the axial stress/particle velocity state (point *B*) of the as-shocked material in the Kevlar-phenolic shell (the region impinged upon by the air-borne blast-wave) is obtained by intersecting the axial stress vs particle velocity Kevlar-phenolic Hugoniot with the mirrored air Hugoniot (where mirroring is carried out about the constant particle-velocity line passing through point *A*). The same procedure is then applied to determine the axial stress/particle velocity as-shocked material states in polyurea internal lining (point *C*), EVA suspension pad (point *D*), skin/fat (point *E*), skull (point *F*), CSF (point *G*) and the cerebrum (point *H*). It should be noted that the Hugoniot relations are represented using solid lines while their mirror images are represented using dashed lines in Figure 15. Also, the Hugoniot curves are not labeled in this figure but their identity can be determined by comparing Figures 14(b) and 15.

Examination of the point *H* results shown in Figure 15 reveal that the predicted negative axial stress and the particle velocity within the cerebrum are 1.75 MPa and

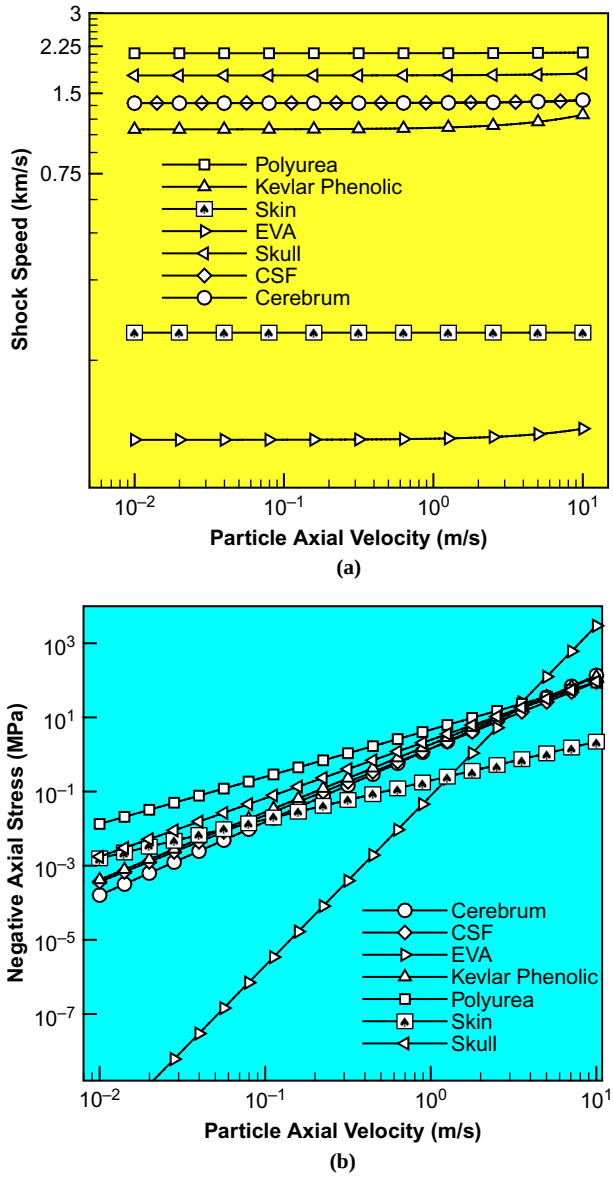

Figure 14.
(a) Shock speed vs particle axial velocity; and (b) negative axial stress vs particle axial velocity Hugoniot relations for the Lagrangian-domain materials used in the present work

1.09 m/s, respectively. These values are considerably higher than their finite element counterparts obtained for the helmet configuration Case E. This finding is expected since the shock impedance-matching technique treats shocks as mathematical discontinuities while the finite element analysis allows for the formation of structured (finite-thickness) shock-waves and for the energy-dissipation induced shock attenuation and dispersion.

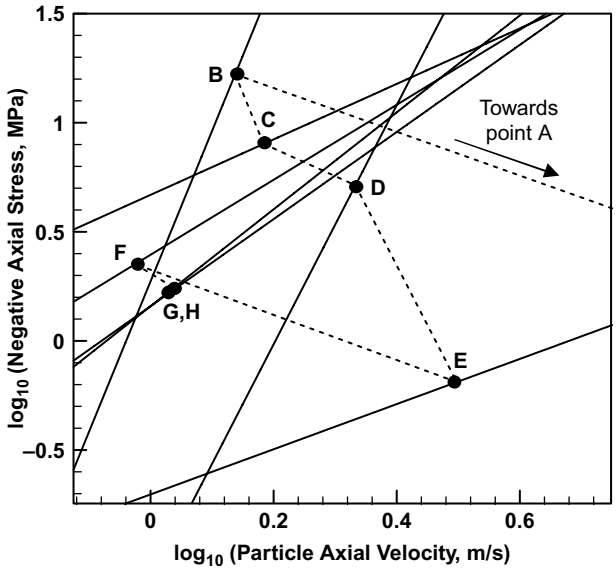

Notes: The corresponding as-shocked material states are represented as: air (point A, not shown for clarity), Kevlar phenolic (point B), polyurea (point C), EVA (point D), skin (Point E), skull (Point F) and CSF (point G); the solid lines in the figure represent Hugoniots while the dashed lines represent the mirror images

Figure 15.
An example of the use of the impedance-matching technique to determine the negative axial stress and particle velocity as-shocked material states in cerebrum (point H) in the case of the ACH helmet augmented through the use of s 2-mm thick polyurea internal lining

Despite the fact that the impedance-matching technique was not able to quantitatively match the finite-element predictions, it is found that it predicted the lowest combination of the axial stress and the particle velocity for the Case E among the six cases analyzed. This finding is fully consistent with the one obtained in the finite-element analysis discussed earlier. As mentioned earlier, a detailed account of the impedance-matching technique used and the experimental results obtained will be presented in our future communication.

4. Summary and conclusions

Based on the results obtained in the present work, the following main summary remarks and conclusions can be drawn:

- A combined Eulerian/Lagrangian fluid/solid transient non-linear dynamics finite element computational analysis of an air/helmet/head core sample is carried out in order to assess the basic shock-mitigation efficacy of a prototypical combat helmet, as related to the prevention of blast-induced mTBI.
- Further improvements in the shock-mitigation efficacy of the combat helmet through the use of polyurea (as suspension pads, internal lining or external coating) are next investigated.
- It is found that the helmet shock-mitigation performance improvements are obtained only in the case of helmet polyurea-based internal lining and that even

these improvements are of a relatively minor extent. Our ongoing preliminary experimental investigation (to be reported in a future communication) supports this finding.

- Application of the impedance matching technique yielded results which, while not being in very good quantitative agreement with the finite element analysis results, correctly predict the relative improvement in the helmet shock-mitigation efficacy through the use of different polyurea-based design alterations.

References

ABAQUS Version 6.10 EF1 (2010), *User Documentation*, Dassault Systems, Velizy-Villacoublay.

ANSYS/Autodyn-2D and 3D, Version 6.1 (2007), *User Documentation*, ANSYS Inc, Canonsburg, PA.

Amini, M.R., Simon, J. and Namet-Nasser, S. (2010), "Numerical modeling of effect of polyurea on response of steel plates to impulsive loads in direct pressure pulse experiments", *Mechanics of Materials*, Vol. 42, pp. 615-27.

Amirkhizi, A.V., Isaacs, J., McGee, J. and Nemat-Nasser, S. (2006), "An experimentally-based viscoelastic constitutive model for polyurea, including pressure and temperature effects", *Phil. Mag.*, Vol. 86 No. 36, pp. 5847-66.

Bhattacharjee, Y. (2008), "Shell shock revisited: solving the puzzle of blast trauma", *Science*, Vol. 319, pp. 406-8.

Cernak, I., Wang, Z., Jiang, J., Bian, X. and Savic, J. (2001), "Ultrastructural and functional characteristics of blast injury-induced neurotrauma", *J. Trauma Injury, Infection, and Critical Care*, Vol. 50 No. 4, pp. 695-706.

Cooper, P.W. (1996), *Explosives Engineering*, Wiley, New York, NY.

Cuitiño, A. and Ortiz, M. (1992), "A material-independent method for extending stress update algorithms from small-strain plasticity to finite plasticity with multiplicative kinematics", *Eng. Comput.*, Vol. 9, pp. 437-51.

Davison, L. (2008), *Fundamentals of Shockwave Propagation in Solids*, Springer, Berlin.

Grujicic, M., Arakere, G. and He, T. (2010a), "Material modeling and structural mechanics aspects of traumatic brain injury problem", *Multidisciplinary Modeling in Materials and Structures*, Vol. 6 No. 3, pp. 335-63.

Grujicic, M., He, T. and Pandurangan, B. (2010b), "Experimental characterization and material-model development for microphase-segregated polyurea: an overview", *Journal of Materials Engineering Performance*, Vol. 21 No. 1, pp. 2-16.

Grujicic, M., Bell, W.C., Pandurangan, B. and Glomski, P.S. (2010c), "Fluid/structure interaction computational investigation of the blast-wave mitigation efficacy of the advanced combat helmet", *Journal of Materials Engineering and Performance*, Vol. 20 No. 6, pp. 877-93.

Grujicic, M., Bell, W.C., Pandurangan, B. and He, T. (2010d), "Blast-wave impact-mitigation capability of polyurea when used as helmet suspension pad material", *Materials and Design*, Vol. 31, pp. 4050-65.

Grujicic, M., He, T., Pandurangan, B., Runt, J., Tarter, J. and Dillon, G. (2011a), "Development and parameterization of a time-invariant (equilibrium) material model for segmented elastomeric polyureas", *Journal of Materials: Design and Applications*, Vol. 225 No. 3, pp. 182-94.

Grujicic, M., Pandurangan, B., Arakere, G., Bell, W.C., He, T. and Xie, X. (2009), "Seat-cushion and soft-tissue material modeling and a finite-element investigation of seating comfort for passenger vehicle occupants", *Materials and Design*, Vol. 30, pp. 4273-85.

Grujicic, M., Pandurangan, B., Bell, W.C., Cheeseman, B.A., Yen, C.-F. and Randow, C.L. (2011b), "Molecular-level simulations of shock generation and propagation in polyurea", *Materials Science & Engineering A*, Vol. 528 Nos 10/11, pp. 3799-808.

Grujicic, M., Pandurangan, B., He, T., Cheeseman, B.A., Yen, C.-F. and Randow, C.L. (2010e), "Computational investigation of impact energy absorption capability of polyurea coatings via deformation-induced glass transition", *Materials Science & Engineering A*, Vol. 527 Nos 29/30, pp. 7741-51.

Grujicic, M., Pandurangan, B., King, A.E., Runt, J., Tarter, J. and Dillon, G. (2010f), "Multi-length scale modeling and analysis of microstructure evolution and mechanical properties in polyurea", *Journal of Materials Science*, Vol. 46 No. 6, pp. 1767-79.

Holm, L., Cassidy, J.D., Carroll, L.J. and Berg, J. (2005), "Neurotrauma task force on mild traumatic brain injury of the WHO collaborating centre: summary of the WHO collaborating centre for neurotrauma task force on mild traumatic brain injury", *J. Rehabil. Med.*, Vol. 37, pp. 131-41.

Hyde, D. (1988), *User's Guide for Microcomputer Programs, CONWEP and FUNPRO – Applications of TM 5-855-1*, US Army Engineer Waterways Experimental Station, Vicksburg, MS.

Moore, D.F., Radovitzky, R., Shupenko, L., Klinoff, A., Jaffee, M.S. and Rosen, J.M. (2008), "Blast physics and central nervous system injury future neurology", *Annals of Neurology*, Vol. 64, p. S30.

Nyein, M.K., Jason, A.M., Yu, L., Pita, C.M., Joannopoulos, J.D., Moore, D.F. and Radovitzky, R.A. (2010), "In silico investigation of intra-cranial blast mitigation with relevance to military traumatic brain injury", *Proc. Natl Acad. Sci., USA*, Vol. 48 No. 107, pp. 20703-8.

Okie, S. (2005), "Traumatic brain injury in the war zone", *New England Journal of Medicine*, Vol. 352, pp. 2043-7.

Taber, K.H., Warden, D.L. and Hurley, R.A. (2006), "Blast-related traumatic brain injury: what is known?", *J. Neuropsychiatry and Clinical Neuroscience*, Vol. 18, pp. 141-5.

Wallsten, S.J. and Kosec, K. (2005), "Social science research network", Paper No. 05-19, available at: http://ssrn.com/abstract=848408

Walsh, S.M., Scott, R.R. and Spagnuolo, D.M. (2005), *The Development of a Hybrid Thermoplastic Ballistic Material with Application to Helmets, ARL-TR-3700*, Army Research Laboratory, Adelphi, MD.

Warden, D. (2006), "Military TBI during the Iraq and Afghanistan wars", *J. Head Trauma Rehab.*, Vol. 21, pp. 398-402.

Corresponding author
M. Grujicic can be contacted at: gmica@clemson.edu